A comparison between low-order and higher-order low-Mach discretization approaches

By S. P. Domino†

A low-order (P=1) generalized unstructured control volume finite element method (CVFEM) that has been deployed for low-Mach Large Eddy Simulations (LES) is extended to a higher-order (P=2) methodology. This promotion of underlying basis provides a formally third-order spatially accurate method. Along with the low- and higher-order CVFEM, a common edge-based scheme is outlined and applied to the low-Mach application space. The three schemes are run on a common code verification problem suite where both error and efficiency findings are provided. The two low-order methods also are modified to allow for a pseudo fourth-order advection operator methodology by the use of projected nodal gradients. Although this method is formally second-order spatially accurate due to Gauss point quadrature error, CVFEM P=1 results indicate a reduction in numerical error with a negligible increase in computational and code complexity cost. Finally, the CVFEM P=2 implementation is shown to perform well in simple verification and vortex traveling flows and represents a viable solution strategy deserving future evaluation for extension to P=3 and beyond.

1. Introduction

The ability to accurately predict the abnormal thermal environment (defined by a highly sooting hydrocarbon combustion event) requires that robust, efficient, scalable and stable methods be deployed. Capturing counter-rotating vortex pairs, which are commonplace in reacting buoyant plumes in cross flow, is key to predicting mixing rates. These Large Eddy Simulations (LES) require methods that provide low dissipation and low dispersive errors. For most general engineering applications of interest, traditional low-order methods require substantial mesh resolution which can provide very large implicit systems. Implicit, higher-order low-Mach discretizations on unstructured meshes are of interest to evaluate for the abnormal thermal LES application space. The efficiency of such higher-order methods compared to, e.g., uniform refinement of low-order methods, is also of interest.

The most common approach for increasing the formal spatial order of accuracy on unstructured meshes is to use the discontinous Galerkin (DG) method (Covello *et al.* 2014). Such higher-order methods are attractive due to the ability to increase the polynomial order to achieve stable and highly accurate solutions. Although the lowest order DG method can be cast as a cell-centered finite volume method, extending a pure cell centered scheme to higher-order representations is somewhat problematic. However, in addition to DG methods, extension of low-order (P=1) control volume finite element implementations has been cited in the literature. For example, a CVFEM higher-order diffusion method has been described (Charoensuk & Vessakosol 2010), although formal order of accuracy results were omitted in the study. Recently, combined approaches of CVFEM

† Computational Thermal and Fluid Mechanics, Sandia National Laboratories

and DG approaches (Discontinous CVFEM) have been used with success for advection-diffusion problems in one-dimensional (Stipcich *et al.* 2011) and two-dimensional applications (Piller & Stalio, 2011). Therefore, the CVFEM approach seems to be a natural candidate to extend to a higher-order method should the interested party desire the features of a finite volume scheme; however, higher-order spatial accuracy is of interest.

In general, investment in low-order, generalized unstructured CVFEM low-Mach algorithms at Sandia National Laboratories has been met with good success. This method has been deployed to support Science-based Stockipe Stewardship within Engineering Sciences (Hanlin *et al.* 2009). Both scalability and stability properties of CVFEM and edge-based vertex-centered (EBVC) methods have been studied. For example, in a recent Sandia study (Lin *et al.* 2014), near-optimal weak scaling in linear solve time and assemble have been demostrated up to 525k core on approximately nine billion element unstructred hex elements. As the laboratory moves towards supporting next-generation platform computing, it is of interest to possibly extend the current low-Mach CVFEM approaches to higher-order implementations as the increased work per element may be attractive on these future generations.

Massively parallel, fully implicit simulations integrating high-fidelity coupled physics are provided through the interface of the application code, Nalu, with the Sierra Toolkit (STK) (Edwards *et al.* 2010) and Trilinos (Heroux *et al.* 2003). The Toolkit is used for core services such as parallel mesh support, topology iteration, ghosting, and field data access. Trilinos is used for parallel sparse solves (both Krylov-based solvers and Algebraic Multi-grid methods) and efficient matrix assembly at scale†.

2. Low-Mach discretization approach

In this preliminary study, the low-Mach fluid equations of motion are solved. The variable density continuity equation is

$$\frac{\partial \rho}{\partial t} + \frac{\partial \rho u_j}{\partial x_j} = 0. \tag{2.1}$$

In the above equation, ρ is the fluids density and u_j is the fluid velocity. The momentum equation solved is

$$\frac{\partial \rho u_i}{\partial t} + \frac{\partial}{\partial x_j} \left(\rho u_j u_i - \sigma_{ij} \right) = S_i. \tag{2.2}$$

Above, the Cauchy stress, σ_{ij}, is

$$\sigma_{ij} = \tau_{ij} - p\delta_{ij} + \frac{2}{3}\mu\frac{\partial u_k}{\partial x_k}\delta_{ij}. \tag{2.3}$$

Each equation is multiplied by a test function, w, and integrated over the domain. For the momentum equation, both the stress and advection are integrated by parts while for the continuity equation, the divergence term is integrated by parts. The integrated-by-parts continuity equation is

$$\int\limits_{\Omega} w\frac{\partial \rho}{\partial t}d\Omega - \int\limits_{\Omega} \frac{\partial w}{\partial x_j}\rho u_j d\Omega + \int\limits_{\Gamma} w\rho u_j d\Gamma - \sum_{elem}\int\limits_{\Omega} \frac{\partial w}{\partial x_j}\tau R_{u_j}d\Omega + \sum_{bc}\int\limits_{\Gamma} wR_{u_j}n_j d\Gamma = 0.$$

In the above equation, τ is the stabilization time scale for the continuity equation and R_{u_j} is the momentum residual applied to the continuity equation. Note that pressure stabilization contributions at exposed surfaces are germane only when open pressure-specified boundaries are present. The integrated-by-parts form of the momentum equation is given by,

$$\int\limits_{\Omega} w\left(\frac{\partial \rho u_i}{\partial t} - S_i\right)d\Omega - \int\limits_{\Omega} \frac{\partial w}{\partial x_j}\left(\rho u_j u_i - \sigma_{ij}\right)d\Omega + \int\limits_{\Gamma} w\left(\rho u_j u_i - \sigma_{ij}\right)d\Gamma = 0.$$

Note that in the above form, there is no explicit residual-based stabilization applied.

2.1. *Test Function Definition*

Following the work of Swaminanthan *et al.* 1993, and also of Martinez 2005, the test function is chosen to be a piecewise-constant value within the control volume, $w = w_I$, and zero outside of this control volume (Heaviside). A key property of this function, as pointed out by Martinez, is that its gradient is a distribution of delta functions on the control volume boundary, $\frac{\partial w_I}{\partial x_i} = -\mathbf{n}_I\delta(\mathbf{x} - \mathbf{x}_{\Gamma_I})$, where $\mathbf{n}_I$ is the outward normal on that boundary. Therefore, the CVFEM and edge-based scheme are naturally categorized as a Petrov-Galerkin method.

Substituting the weight function relationship into the residual equation provides the final form of vertex-centered finite volume equation (not shown due to space constraints). Frequently, finite volume methods simply apply Gauss-divergence to arrive at the final integral form of the working equations. However, the above description naturally allows for residual-based approaches to be described.

2.2. *CVFEM dual mesh*

The classic low-Mach algorithm uses the finite volume technique known as the control volume finite element method (Schneider & Raw, 1987). Control volumes (the mesh dual) are constructed about the nodes as shown in Figure 1(a). Each element contains a set of sub-faces that define control volume surfaces. These sub-faces consist of line segments (two-dimensional) or surfaces (three-dimensional). The two-dimensional segments are connected between the element centroid and the edge centroids. The three-dimensional surfaces are connected between the element centroid, the element face centroids, and the edge centroids. Integration points also exist within the subcontrol volume centroids. The collection of all elements touching a node defines the full control volume. For residual and matrix evaluations, the topology by which one loops is the element (interior contributions) and boundary faces (boundary condition contributions). Note that while this element type is overintegrated, i.e., two integration points are used for each complete sub-face, integration points remain at the centroid of the sub-faces.

The quadratic CVFEM element is described in Figure 1(b). In this element type, the linear basis (P=1) is promoted to a quadratic (P=2). The nodes per element increase from four to nine in two-dimensional and eight to 27 in three-dimensional. However, the standard P=1 quadrature points must be both shifted and augmented such that two integration points exist per sub-face within the element. Moreover, in order to retain

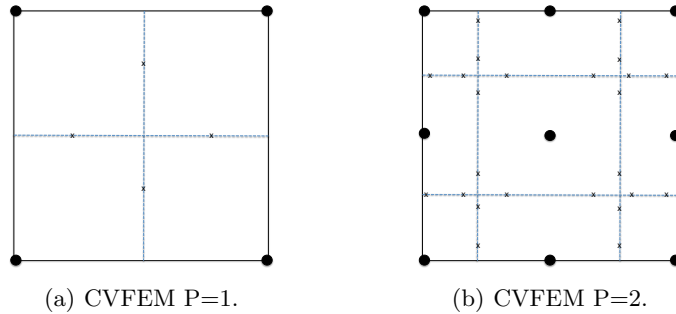(a) CVFEM P=1.   (b) CVFEM P=2.

FIGURE 1. Dual mesh defined for the two-dimensional CVFEM quad element.

the higher-order accuracy, Gauss quadrature (2x2 integration) is required. This finding
has been omitted in the small subset of higher-order CVFEM approaches outlined in the
literature (e.g., Charoensuk & Vessakosol 2010); however, it is critical to exactly integrate
a quadratic over the element sub-faces.

When using the CVFEM, the discretized equations described in this paper are evalu-
ated at either subcontrol surface integration points (terms that have been integrated by
parts) or at the subcontrol volume Gauss points (time and source terms). Interpolation
within the element is obtained by the standard elemental basis functions,

$$\phi_{ip} = \sum N_k^{ip} \phi_k. \tag{2.4}$$

where the index k represents a loop over all nodes in the element. Gradients at the
subcontrol volume surfaces are obtained by taking the derivative of Eq. 2.4, to obtain

$$\frac{\partial \phi_{ip}}{\partial x_j} = \sum \frac{\partial N_{j,k}^{ip}}{\partial x_j} \phi_k. \tag{2.5}$$

Full linear and higher-order elements exist for hex, tet, pyramid, wedge, tri, and quad
topologies. In this preliminary scoping study, the two-dimensional quad topology was
used. However, the design of the CVFEM code structure is polymorphic in nature. The
specialty algorithmic code remains the same as new topological integration rules are
added to the set of supported master elements. Therefore, extension to other topologies
is straightforward as only geometry-like classes must be implemented.

2.3. *EBVC discretization*

In the edge-based discretization, the dual mesh defined by the CVFEM approach is used
to pre-process both dual mesh nodal volumes (needed in source and time terms) and
edge-based area vectors (required by the integrated-by-parts terms, e.g., advection and
diffusion). Consider the linear element described in Figure 1(a). The quadrature points for
integrated-by-parts quantities are shifted to the edge midpoint. Moreover, the area vector
at the sub-faces is assembled to the edge midpoint. In an edge-based scheme, the time
and source terms use single-point quadrature by assembling the subcontrol volumes to a
single nodal control volume. The consolidation of advection/diffusion contributions to the
edge midpoint and the time/source terms to nodal locations results in a canonical five-
point and seven-point stencil for two-dimensional and three-dimensional, respectively.

This reduction of matrix size and simple data access pattern (nodes and edges) makes this scheme highly efficient.

2.4. *Discretization approaches for key terms*

In this section, the approach used for pressure stabilization, time, source, projected nodal gradients, and advection operator approaches are overviewed.

2.4.1. *Pressure stabilization*

Equal order interpolation for the primitives (velocity and pressure) requires the usage of pressure stabilization (Domino 2008). Although there are many ways in which this stabilization approach can be described (Domino 2006), the prime goal is the same: avoid the null space in the coupled equations of motion by adding a Laplacian operator of pressure within the continuity equation. Specifically, a higher-order pressure dissipation term is added to the continuity equation that can either arise from a special velocity interpolation method or through a fine-scale momentum residual. In this study, we prefer to describe the pressure stabilization in the class of residual-based approaches in which a scaled momentum residual is added to the continuity equation (Swaminanthan *et al.* 1993). The order of the scheme used in the momentum equation is, therefore, retained in the extra residual added to the continuity system. It is through the pressure gradient term in momentum that the classic pressure Poisson equation is obtained. The coupled system is split and solved using an incremental approximate pressure projection method (Domino 2006).

2.4.2. *Projected nodal gradients*

In the edge- or element-based algorithm, projected nodal gradients are commonplace, e.g., the pressure stabilization term, higher-order upwind methods, turbulence source terms and for the pseudo higher-order advection operator calculation. For an edge-based scheme, they are also used in the diffusion term when non-orthogonality of the mesh is noted. In this study, projected nodal gradients are determined by an L2 projection where integration points are either at the subcontrol surface or the edge midpoint.

2.5. *Time and source terms*

Time and source terms, i.e., volumetric contributions, are applied at the dual nodal volume integration points. In the CVFEM approach, a consistent mass matrix or lumped approach can be used. For the EBVC scheme, in order to avoid stencil bloat, the lumped mass approach is used. Time discretization uses the three-state BDF2 scheme.

2.6. *Diffusion*

For the CVFEM approach, the diffusion term at the subcontrol surface integration points use the the elemental shape functions and derivatives (Eqs. (2.4) -(2.5)) . For the edge-based diffusion operator, special care is noted as there is no ability to use the elemental basis to define the diffusion operator. As with cell-centered schemes, non-orthogonal contributions for the diffusion operator arise due to a difference in direction between the assembled edge area vector and the distance vector between nodes on an edge. On skewed meshes, this non-orthogonality cannot be ignored. Following the work of Jasak 1996, the over-relaxed approach is used.

2.7. *Advection operator*

A generic advection contribution for primitive ϕ is $ADV_\phi = \int \rho u_j \phi_{ip} n_j dS = \sum \dot{m} \phi_{ip}$. When avoiding residual-based methods, the evaluation of ϕ_{ip} defines the advection sta-

bilization choice. In general, the advection choice is a cell Peclet blending between dissipative higher-order upwind (ϕ_{upw}) and a low dissipation generalized central (Galerkin) operator, ϕ_{gcds}, i.e., $\phi_{ip} = \eta\phi_{upw} + (1 - \eta)\phi_{gcds}$.

For low-Mach LES applications, it is generally required to add very little to no explicit dissipation ($\eta = 0$). In the above equation, η is a cell Peclet blending where values of unity represent full higher-order upwind while values closer to unity result in pure central. When upwind dissipation is completely removed, the generalized central operator (ϕ_{gcds}) can take on a pure form of second-order accurate (P=1), third-order accurate (P=2) or a pseudo fourth-order form in which projected nodal gradients are used to construct higher-accuracy Galerkin operator depending on a user-controlled parameters (α).

The upwind operator, ϕ_{upw}, is computed based on a blending of the extrapolated state (using the projected nodal gradient) and the linear interpolated state. Second- or third-order upwind is provided based on the value of α_{upw} blending.

$$\phi_{upw} = \alpha_{upw}\tilde{\phi}^L_{upw} + (1 - \alpha_{upw})\,\phi_{cds};\ \dot{m} > 0,$$
$$\alpha_{upw}\tilde{\phi}^R_{upw} + (1 - \alpha_{upw})\,\phi_{cds};\ \dot{m} < 0. \tag{2.6}$$

The extrapolated value based on the upwinded left (ϕ^L) or right (ϕ^R) state is

$$\tilde{\phi}^L_{upw} = \phi^L + d^L_j G_j \phi^L,\ \tilde{\phi}^R_{upw} = \phi^R - d^R_j G_j \phi^R.$$

The distance vectors are defined based on the distances between the L/R points and the integration point (edge- or element-based), $d^L_j = x^{ip}_j - x^L_j$ and $d^R_j = x^R_j - x^{ip}_j$.

Second- (P=1) or third-order (P=2) Galerkin is outlined in Eq. 2.4, where N^{ip}_k is evaluated at either the subcontrol surface or the edge midpoint and ϕ_k is the nodal value. In the case of the edge-based scheme, the midpoint evaluation provides for a skew-symmetric form of the operator.

The generalized central difference operator is provided by blending with the extrapolated values and second-order Galerkin,

$$\phi_{gcds} = \frac{1}{2}\left(\hat{\phi}^L_{upw} + \hat{\phi}^R_{upw}\right), \tag{2.7}$$

where

$$\hat{\phi}^L_{upw} = \alpha\tilde{\phi}^L_{upw} + (1 - \alpha)\,\phi_{cds},$$
$$\hat{\phi}^R_{upw} = \alpha\tilde{\phi}^R_{upw} + (1 - \alpha)\,\phi_{cds}. \tag{2.8}$$

When using the low-order methods, the value of α provides the type of pseudo fourth-order stencil. However, due to quadrature error, this scheme is not formally fourth-order accurate (as will be demonstrated in the verification section). Moreover, on a general unstructured mesh, the idealized one-dimensional stencil is lost. Nevertheless, this method will be shown to reduce the numerical error at very little computational expense.

The above set of advection operators can be used to define an idealized one-dimensional stencil denoted by ($i - 2$, $i - 1$, i, $i + 1$, $i + 2$), where i represents the particular row for the given transported variable. For example, a value of $\alpha = \frac{1}{2}$ provides a 1D stencil of: ($\frac{1}{8}, -\frac{6}{8}, 0, \frac{6}{8}, -\frac{1}{8}$) whereas a value of $\alpha = \frac{2}{3}$ results in a 1D stencil of: ($\frac{1}{12}, -\frac{8}{12}, 0, \frac{8}{12}, -\frac{1}{12}$). In most practical engineering problems of interest, this idealized stencil is rarely achieved. The value of α_{upw} determines whether or not second-order From's method or third-order upwind is used.

3. Discussion on order of accuracy

For the unsteady isothermal, uniform laminar physics set, the exact solution of the convecting, decaying Taylor vortex is used. This analytical solution is ideal in that quadrature error due to source evaluation is removed. The equation set is

$$u = u_o - cos(\pi(x - u_o t))sin(\pi(y - v_o t))e^{-2.0\omega t},$$
$$v = v_o + sin(\pi(x - u_o t))cos(\pi(y - v_o t))e^{-2.0\omega t},$$
$$p = -\frac{p_o}{4}(cos(2\pi(x - u_o t)) + cos(2\pi(y - v_o t)))e^{-4\omega t}. \tag{3.1}$$

The constants u_o, v_o, and p_o are all assigned values of 1.0; the viscosity μ is set to a constant value of 0.001 which results in a cell Reynolds number of 20. The value of ω is $\pi^2\mu$.

To demonstrate temporal accuracy for P=2 CVFEM, the simulation is marched out to a fixed time of 1 second where temporal errors are computed. Since the expected order of accuracy of the temporal scheme is second-order and the anticipated order of accuracy for the spatial scheme is third-order accurate, the time step is reduced by a factor of $\frac{1}{2\sqrt{2}}$. Therefore, the error is expected to drop by a factor of eight for each simulation run. Figure 2(a) demonstrates the second-order temporal error for the velocity field CVFEM P=2 approach. Temporal accuracy results for the P=1 methods are previously outlined in the formal Nalu code verification document (Domino 2014).

For the spatial order of accuracy study, the same transient analytical solution is used. A sufficiently small time step is chosen for all mesh sizes to ensure that the temporal accuracy error is very small relative to the spatial errors. In this case, a time step of 1.0e-4 was used that corresponded to a Courant number of 0.02 on the coarse P=1 mesh. Figure 2(b) illustrates the spatial order of accuracy for the baseline P=1 methods (both CVFEM and EBVC) to be second-order and third-order for the P=2 CVFEM. Based on the spatial error plots, the finest P=1 method compares closely to the coarsest P=2 mesh.

To illustrate the effect of the pseudo fourth-order approach, Figure 2(c) outlines the pseudo fourth-order approach applied to the P=1 CVFEM as compared to the baseline P=1 and P=2 CVFEM. The value of α is either $\frac{1}{2}$ or $\frac{2}{3}$. Results indicate formal second-order accuracy for this pseudo fourth-order scheme with a slight reduction in error norms relative to the baseline P=1 CVFEM.

4. A Note on performance

Although the error reduction of the new P=2 CVFEM approach is highly attractive, a brief survey of the code timings is presented in order to provide context on algorithmic efficiency. The test case highlighted is a traveling inviscid vortex (Nordstrom *et al.* 2009) in which an initial condition for velocity and pressure is advected downstream. In this test case case the diffusion terms are included and the viscosity is set to standard viscous conditions of air. Four methods are compared: the P=1 CVFEM, P=1 EBVC, P=1 CVFEM with $\alpha = \frac{1}{2}$, and, finally, the P=2 CVFEM. In this study, the total assembly and solve time for momentum and continuity and the linear iterations for each system solve are provided in Table 1; values are nomalized relative to the P=1 CVFEM.

The results captured in the scaled data table clearly show an increased assembly cost for the higher-order method. Although the momentum iteration count is well behaved, the
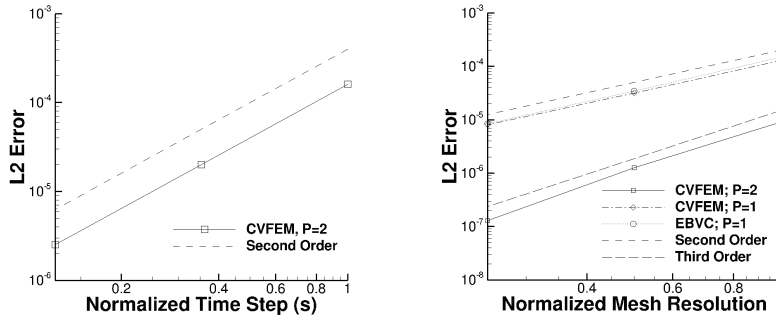
(a) Temporal error, CVFEM P=2.   (b) Spatial error, CVFEM/EBVC.
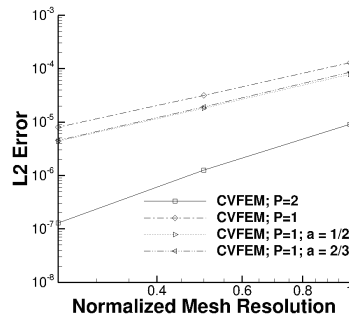
(c) Spatial error, pseudo 4th.

FIGURE 2. Velocity order of accuracy for the full suite of methods.

number of linear iterations for the continuity pressure Poisson solve increases by almost a factor of five. Overall, the timing for the higher-order method is less than 2x slower. In this study, the continuity matrix preconditioner was re-initialized at each of the 1000 time steps. Moreover, there was no advanced interface implemented for the GMRES solver and multilevel preconditioner. It is anticipated that preconditioning the lower-order system and prolongation back to the higher-order system will reduce the setup time with some cost to Poisson linear iterations. No special care seems to be required for the non-eliptic systems. As expected, the P=1 EBVC scheme is the fastest method.

Timing	CVFEM P=1; $\alpha = \frac{1}{2}$	EBVC $\alpha = 0$	CVFEM P=2 $\alpha = 0$
Cont Assemble	0.998	0.706	1.481
Cont Solve	1.526	0.701	1.739
Cont Iter	1.667	0.924	4.658
Mom Assemble	1.000	0.796	1.483
Mom Solve	0.995	1.158	2.130
Mom Iter	1.000	0.936	1.001
Total	1.208	0.605	1.704

TABLE 1. Scaled results for CVFEM P=1, $\alpha = \frac{1}{2}$; EBVC P=1,$\alpha = 0$; and CVFEM P=2 $\alpha = 0$ relative to CVFEM P=1, $\alpha = 0$.

5. Conclusions

A novel third-order spatially accurate and second-order temporally accurate CVFEM has been implemented and tested within a massively parallel, generalized unstructured low-Mach reacting flow code base, Nalu. This scheme naturally fits within an already existing element-based CVFEM implementation by the definition of a new element topology. Results indicate that this new higher-order low-Mach fluids method provides a competitive solution time relative to its lower order CVFEM and EBVC counterparts. More work is required to understand scalability and stability of this new scheme. Stability properties for simulations that include passive transport or turbulence quantities are planned, as is improvement of the continuity solve. Extension to higher-order (P=3 and beyond) is also possible and of interest. However, mesh generation and consolidation of shared degree-of-freedoms at element faces must be addressed should the non-discontinuous approach remain the desired path forward.

REFERENCES

COVELLO, V, NIGRO, A., DEBARTOLO, C. AND G. FLORIO 20014 Discontinuous Galerkin solutions of internal low-Mach number turbulent flows. *Energy Procedia*, **45** 528–537.

Nordstrom, J., Hamm, F., Shoeybi, M, van der Weide, E., Svard, M., Mattsson, K, Iaccarino, G and J. Gong 20010 A hybrid method for unsteady inviscid flow. *Comput. Fluids*, **38** 875–882.

Charoensuk, J and P. Vessakosol 2010 A high order control volume finite element method procedure for transient heat conduction analysis of functionally graded materials. *Heat Mass Transfer.*, **46** 1261–1276.

Domino, S. P. 2006 Towards verification of formal time accuracy for a family of approximate projection methods using the method of manufactured solutions. *Proceedings of the Summer Program*, Center for Turbulence Research, Stanford University, pp. 163–177.

Domino, S. P. 2008 A comparison of various equal-order interpolation methodologies using the method of manufactured solutions. *Proceedings of the Summer Program*, Center for Turbulence Research, Stanford University, pp. 97–111.

Jasak, H. 1996 *Error analysis and estimation for the finite volume method with applications to fluid flow.* Ph.D. Thesis, Imperial College.

Domino, S. P. 2014 *Sierra low-Mach Module Nalu: Code verification manual.* Sandia National Laboratories Internal Report.

Lin, P., Bettencourt, M., Domino, S., Fisher, T., Hoemmen, M., Hu, J., Phipps, E., Prokopenko, A., Rajamanickam, S., Siefert, C. and S. Kennon 2014 Towards extreme-scale simulations for low-Mach fluids with second-generation Trilinos. *Parallel Process. Lett.* (Invited Article).

Martinez, M. 2005 Comparison of Galerkin and control volume finite element for advection-diffusion problems. *Int. J. Num. Meth. Fluids*, **50** 347–376.

Schneider, G. E. and M. J. Raw 1987 Control volume finite element method for heat transfer and fluid flow using colocated variables 1.) computational procedure. *Num. Heat Trans.*, **11** 363–390.

Swaminanthan, C. R., Voller, V.R. and S. V. Patankar 1993 A streamline upwing control volume finite element methods for modeling fluids flow and heat transfer problems. *Finite Elem. Anal. Des.*, **13** 169–184.

Stipcich, G., Piller, M., Pivetta, M. and L. Zovatto 2011 Discontinuous control-volume/finite-element method for advection-diffusion problems. *Comput. Fluids*, **52** 33–49.

Piller, M & E. Stalio 2011 Development of a mixed control volume - Finite element method for the advection-diffusion equation with spectral convergence. *Comput. Fluids*, **40** 169–279.

Heroux, M., Bartlett, R., Howle, V., Hoekstra, R., Hu, J., Kolda, T., Lehoucq, R., Long, K., Pawlowski, R., Phipps, E., Salinger, A., Thornquist, J, Tuminaro, R., Willenbring, J. and A. Williams 2003 An overview of Trilinos. *Sandia National Laboratories SAND Series*, SAND2003-2927.

Hanlin, A., Domino, S. P., Figueroa, V. and V. Romero 2009 Validation and uncertainty quantification of Fuego simulations of calorimeter heating in a wind-driven hydrocarbon pool fire. *Sandia National Laboratories SAND Series*, SAND2009-7605.

Edwards, H. C., Williams, A. B., Sjaardema, G. D., Baur, D. G. and W. K. Cochran 2010 SIERRA Toolkit computational mesh computational model. *Sandia National Laboratories SAND Series*, SAND2010-1192.